ISSN (Print) 1226-1750
ISSN (Online) 2233-6656
Journal of Magnetics 30(4), 651-659 (2025) https://doi.org/10.4283/JMAG.2025.30.4.651

Evaluation of Composite Lead-Free Shield for Clinical Use in C-Arm Fluoroscopy

Jung Ju Jo[1,2], Kum Bae Kim[1,2,3], Yoon Ho Shin[4], and Sang Hyoun Choi[1,2,3]*

[1]*Radiological & Medical Sciences, University of Science and Technology, Seoul 34113, Republic of Korea*
[2]*Radiation Therapy Technology and Standards, Korea Institute of Radiological and Medical Sciences, Seoul 01812, Republic of Korea*
[3]*Department of Radiation Oncology, Korea Institute of Radiological & Medical Sciences, Seoul 01812, Republic of Korea*
[4]*Medical Device Development Center, Daegu-Gyeongbuk Medical Innovation Foundation, Daegu 41061, Republic of Korea*

(Received 14 November 2025, Received in final form 15 December 2025, Accepted 16 December 2025)

C-arm fluoroscopy provides essential real-time imaging for various interventional procedures but entails radiation exposure risks for both patients and medical staff. Conventional lead and lead-free shields offer high attenuation yet remain limited in clinical use due to weight, image artifacts, and procedural constraints. This study evaluated a lead-free composite shield composed of tungsten, tungsten carbide, bismuth, aluminum, and polyurethane, focusing on dose reduction, scatter shielding performance, image quality, and interactions with Automatic Brightness Control (ABC) in a C-arm environment. PHITS-based Monte Carlo simulations demonstrated strong attenuation in the low-to-mid energy range across 60–120 kVp. Experimental measurements showed attenuation rates of 59.6–70.8% (no filter), 45.4–55.4% (Al 2.5 mm), and 37.5–49.5% (Cu 0.25 mm), corresponding to 0.04 mmPb. Scattered radiation shielding efficiency ranged from 36–58% (1 layer) and 61–80% (1.5 layers). Phantom tests confirmed an average 29% dose reduction without significant ABC-driven parameter increases, and SNR/CNR changes were not statistically significant ($p > 0.05$).

Keywords : electromagnetic wave, lead-free shield, c-arm fluoroscopy, dose reduction

1. Introduction

C-arm X-ray systems are widely utilized as essential equipment for providing real-time fluoroscopic imaging during various interventional procedures, including orthopedic, neurosurgical, pain management, and vascular interventions [1, 2]. The X-rays generated by C-arm systems are a form of electromagnetic radiation, and their high photon energy allows them to ionize matter. As these high-energy X-rays pass through the human body, differences in tissue density and effective atomic number cause attenuation, forming the basis of image generation. Consequently, image quality is determined by the intensity and energy spectrum of the incident X-rays, as well as the attenuation characteristics of human tissues [3-5].

C-arm fluoroscopy is used not only for diagnostic purposes but also as a real-time imaging guide during surgical and interventional procedures. Prolonged or repeated exposure can result in cumulative patient doses ranging from several hundred μSv to several mSv [6]. Such exposure includes not only primary radiation but also scattered radiation generated from interactions with tissues, which poses additional risks—particularly for radiosensitive organs such as the thyroid, breast, and gonads, where cumulative doses may increase the likelihood of radiation-induced conditions [7, 8].

To reduce patient radiation exposure, modern C-arm systems are equipped with Automatic Brightness Control (ABC), which adjusts radiation output based on patient thickness or density. The ABC system automatically regulates tube voltage (kVp), tube current (mA), and pulse width to maintain consistent image brightness and quality [9]. Although ABC primarily aims to ensure consistent image quality, its capability for active optimization to minimize patient dose remains limited [10].

Healthcare personnel typically employ protective measures such as lead aprons, thyroid shields, and mobile radiation shields; however, radiation protection for patients remains relatively insufficient due to concerns about potential degradation of image quality [11-13]. Although numerous studies have attempted to adapt lead-based shields—traditionally used for staff protection—for patient use,

*Corresponding author: Tel: +82-2-970-1590
e-mail: shchoi@kirams.re.kr

conventional lead shields exhibit limited clinical applicability because of their weight, image artifacts, discomfort during application, and restricted usability around the procedural site [14, 15]. For example, Lestari *et al.* reported up to a 38% reduction in breast dose using a lead–silicone rubber shield, but image artifacts degraded diagnostic quality, ultimately limiting clinical use [16].

To overcome the limitations of lead-based shields, research has focused on developing lightweight, lead-free shielding materials such as bismuth [17-19]. Kawauchi *et al.* demonstrated approximately 26% dose reduction using a bismuth shield, yet decreases in image contrast and increases in noise were also observed, indicating compromised image quality [20]. Furthermore, although several studies have investigated the feasibility of applying both lead and lead-free shields to patients, an AAPM report highlighted that when shields overlap the exposure field in systems using Automatic Exposure Control (AEC), tube voltage and current may increase, potentially raising patient dose instead [21].

These previous studies suggest that existing shielding materials have not sufficiently achieved a balance between maintaining image quality and reducing radiation exposure. Therefore, to overcome the limitations identified in earlier research, we developed a diagnostic composite shield by combining tungsten, tungsten carbide, bismuth metal, aluminum, and polyurethane, integrating the physical advantages of each constituent material. By evaluating the physical performance of the fabricated shield, its effectiveness in attenuating scattered radiation, and its impact on image quality, this study aims to demonstrate the clinical applicability of the composite shield for effectively reducing radiation exposure during C-arm examinations while preserving diagnostic image quality.

2. Materials and Methods

2.1. Radiation Shield for C-Arm Fluoroscopy

The radiation shield for image interpretation was composed of tungsten, tungsten carbide, bismuth, aluminum, and polyurethane, with a shielding layer thickness of 0.24 mm, and featured a homogeneous single-layer structure with a total areal density of 0.09 g/cm². As shown in Fig. 1, nonwoven fabric and sponge layers were added, resulting in total thickness of approximately 5 mm. Among the shield components, tungsten and tungsten carbide serve as the primary attenuation materials due to their high atomic numbers, while bismuth and aluminum were incorporated to enhance low-energy attenuation efficiency and mechanical strength.

2.2. Monte Carlo Simulation

To evaluate the energy-dependent photon attenuation characteristics of the composite shield, numerical simulations were performed using PHITS (Particle and Heavy Ion Transport code System, ver. 3.341). This analysis was conducted to assess how the combination of constituent materials influences photon fluence and absorbed dose across varying tube voltages (60–120 kVp). X-ray spectra were generated using SpekCalc v1.1 under conditions of 60, 80, 100, and 120 kVp, with a target angle of 15°, and inherent filtration of 0.8 mm beryllium, 1 mm aluminum, and 0.11 mm copper (Fig. 2). These spectra were imported into PHITS as input data. To sufficiently collimate the X-rays and narrow the beam width, a tungsten collimator with a 10 × 10 cm² opening and a thickness of 4 cm was modeled, and the shield was placed 100 cm from the source as shown in Fig. 2. In PHITS, the shielding material was modeled as a homogeneous single substance using the relative mass fractions of tungsten, tungsten

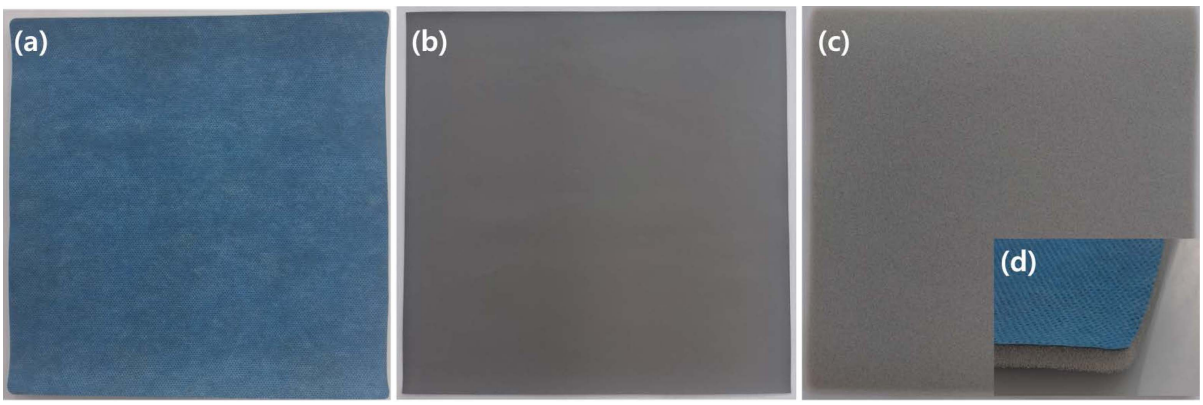

Fig. 1. (Color online) Components of the shield structure. (a) Nonwoven fabric layer on the surface of the shield, (b) Shielding layer composed of composite materials, and (c) Sponge layer for maintaining the shield's shape and ease of use.

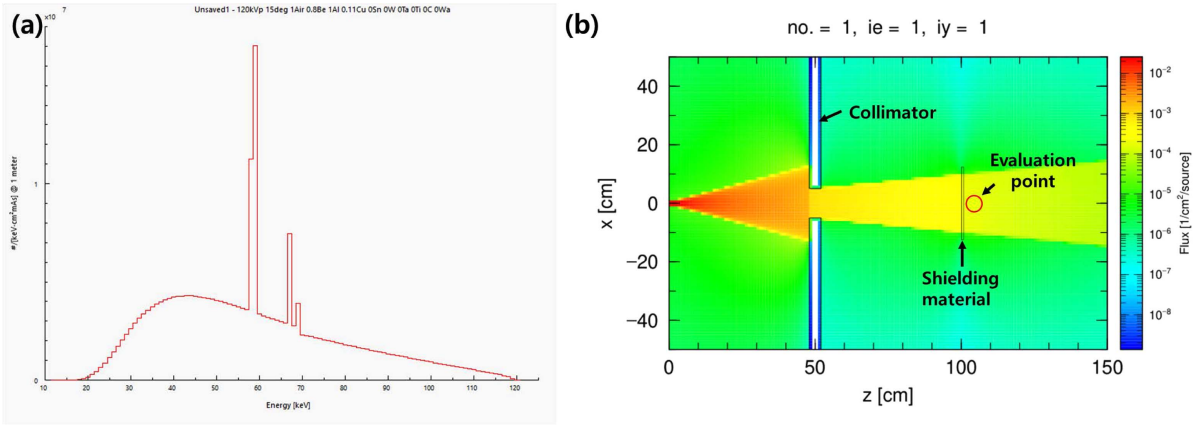

Fig. 2. (Color online) (a) Construction of the SpekCalc energy spectrum, and (b) PHITS Monte Carlo simulation geometry.

carbide, bismuth, aluminum, and polyurethane (normalized to unity), and the shield was implemented as a 25 × 25 cm² slab. The energy spectrum of the X-rays transmitted through the collimator and the shield was analyzed in terms of the flux values [1/cm²/MeV/source], with the scoring position defined immediately beyond the shielding material.

2.3. Shielding Efficiency

To evaluate the shielding efficiency of the shield, an MXR-320/26 X-ray generator (Comet AG, Wünnewil-Flamatt, Switzerland) at an internationally accredited testing laboratory was used. Measurements were performed under the narrow-beam conditions specified in the Korean Industrial Standard for lead equivalence testing of X-ray protective devices (KS A 4025:2017), at tube voltages of 60, 80, 100, and 120 kVp with 20 mAs, and each condition was repeated five times. A calibrated Radcal 10X6-6 CT ionization chamber (Radcal Corporation, Monrovia, CA, USA) was used as the measuring device. The shielding efficiency was measured with and without additional filters of 2.5 mm Al and 0.25 mm Cu, and the lead equivalence was calculated by comparing the measured attenuation values with reference attenuation results obtained using lead of various thicknesses (Fig. 3). The shielding efficiency was calculated using the average dose measured without the shield and the average dose measured after transmission through the shield.

2.4. Scattered Radiation Measurement

To assess the shielding performance against scattered radiation generated through X-ray interactions with the human body, the scattered radiation shielding rate was measured. The measurements were performed using the same X-ray generator described above. The distance between the source and the detector was set to 1 m, and

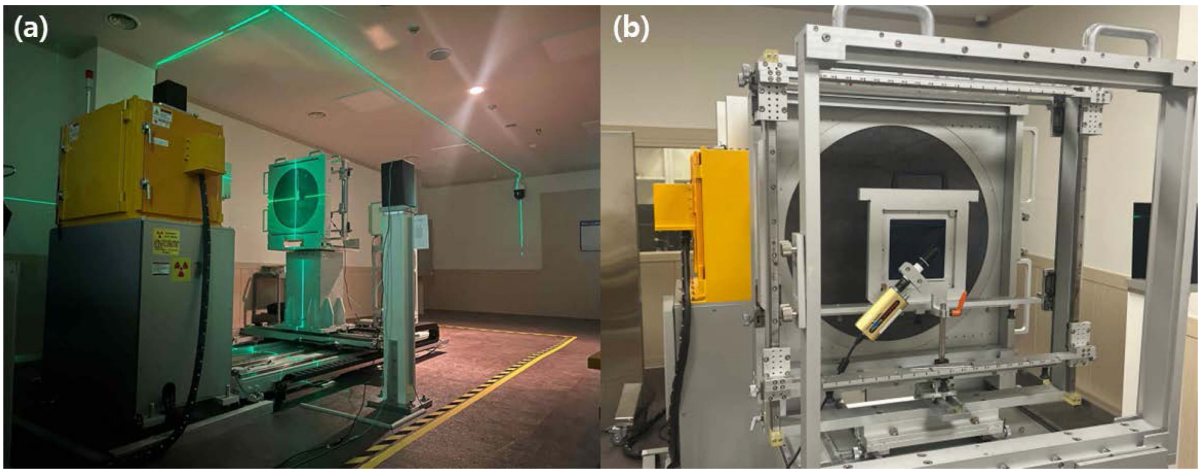

Fig. 3. (Color online) (a) Standard X-ray generation system, and (b) Test environment for radiation-shielding devices.

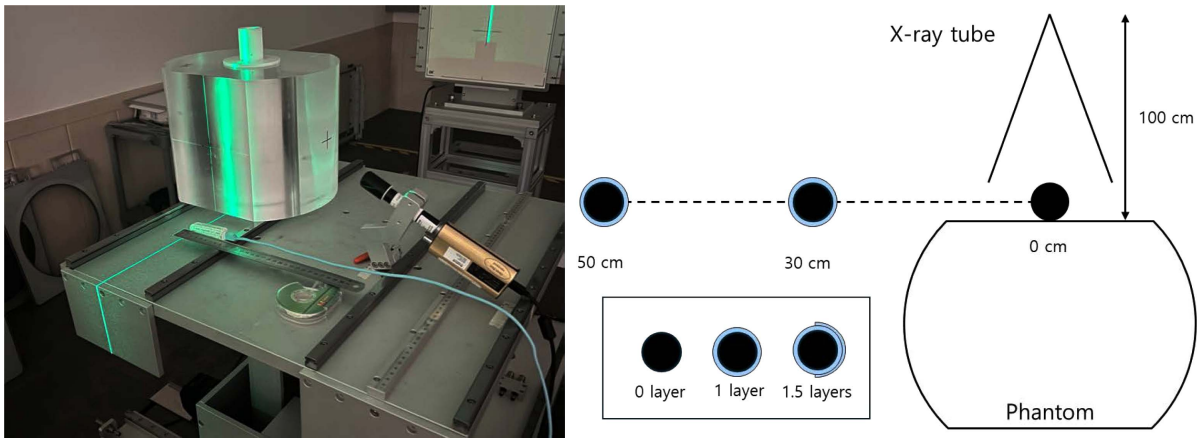

Fig. 4. (Color online) Schematic diagram and evaluation photographs of scattered radiation measurements.

the irradiation field was configured as a circular beam with a diameter of 20 cm. An in-house acrylic phantom measuring 30 × 30 × 25 cm was used. A 2.5 mm Al additional filter was applied, and the tube voltage and current were set to 60–120 kVp and 10 mA, respectively. The same calibrated ionization chamber used for the shielding efficiency evaluation was employed. To ensure effective attenuation of scattered radiation, the shield was enclosed around the detector as illustrated in Fig. 4. Measurements were performed under three shielding configurations, namely without the shield (0 layer), with a complete 360-degree wrap corresponding to one layer, and with one full wrap plus an additional 180-degree overlap corresponding to one and a half layers. The measurement positions were set at 30 cm and 50 cm from the center of the primary beam, and each configuration was repeated five times to obtain the mean values.

2.5. Image Acquisition and Dose Measurement

Phantom experiments were conducted to quantitatively evaluate the dose reduction effect and changes in image quality when the composite shield was used under conditions in which the Automatic Brightness Control (ABC) of the C-arm system was activated. Dose reduction was assessed in fluoroscopy mode using a Zen-2090 Turbo C-arm system (Genoray, Korea) with the ABC function enabled. An in-house chest phantom composed of tissue-equivalent material and a calibrated Raysafe 452 dosimeter (Unfors RaySafe, Sweden) were used. As shown in Fig. 5, the shield was placed between the X-ray source and the phantom, and the radiation dose was measured using a dosimeter positioned on top of the phantom. To induce variations in ABC-regulated tube voltage, fluoroscopy was performed by positioning the thicker portion of the phantom to generate higher kVp

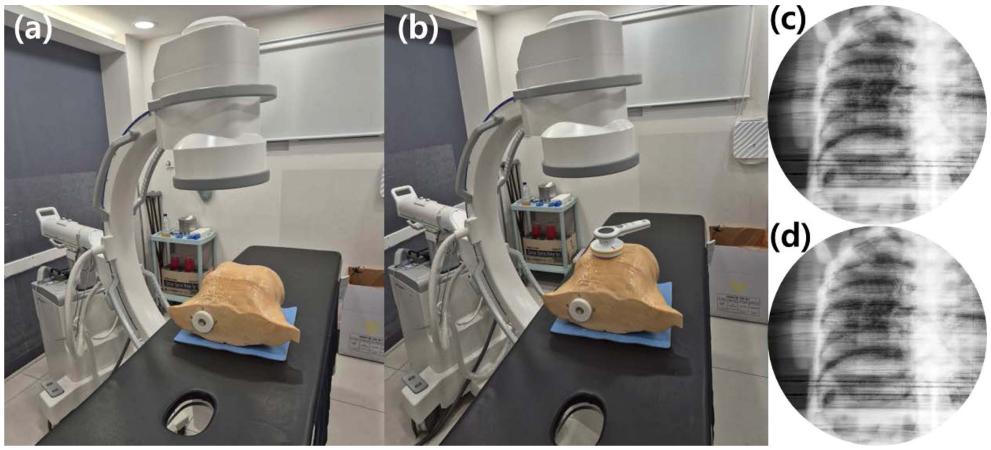

Fig. 5. (Color online) (a) Phantom and shield setup for image acquisition, (b) phantom–shield–dosimeter setup for dose evaluation, (c) C-arm image of the phantom without shield, and (d) C-arm image of the phantom with shield.

conditions and the thinner portion to generate lower kVp conditions. For comparative evaluation with and without the shield, each measurement condition was repeated three times. The average changes in tube voltage, tube current, and measured exposure dose were then analyzed to calculate the relative dose reduction rate.

Quantitative image quality was assessed using the Signal-to-Noise Ratio (SNR) and Contrast-to-Noise Ratio (CNR). SNR was calculated using the mean pixel value and standard deviation (noise) of the target region, as described in Equation (1). CNR was calculated using the mean value of the target region, and the mean value and standard deviation (noise) of air, as shown in Equation (2). For this analysis, ROIs were placed in a homogeneous area of the lung parenchyma (target) and a uniform air region (background). A total of four radiographic images were used (with and without shield), and five ROI pairs were extracted from each image, yielding 20 SNR/CNR data points. Identical ROI positions and sizes were applied across all images to ensure consistency. Differences in SNR and CNR before and after applying the shield were analyzed using paired t-tests, and the Wilcoxon signed-rank test was used when the data did not satisfy normality assumptions. All statistical tests were performed using a two-tailed significance level of $p < 0.05$.

$$SNR = \frac{mean_{target}}{Noise_{target}} \tag{1}$$

$$CNR = \frac{HU_{target} - HU_{BKG}}{\sqrt{\frac{Noise_{target}^2 + Noise_{BKG}^2}{2}}} \tag{2}$$

3. Results

3.1. Radiation Shielding Characteristics

Using PHITS simulations, the energy-dependent dose reduction rates were analyzed according to changes in tube voltage and the application of the shield. The variations in the energy spectrum with and without the shield are shown in Fig. 6, and the shielding efficiency generally decreased across energy ranges as the tube voltage increased. In the 10–20 keV range, shielding efficiency remained nearly identical across all tube voltages, ranging from 99.1% to 100%. In the 30–40 keV range, differences between tube voltages were minimal, with values of 88.3–88.4% at 30 keV (120–60 kVp) and 66.5–67.3% at 40 keV (120–60 kVp). At 50 keV, the shielding efficiencies were 48.7%, 43.8%, 40.3%, and 38.6% for 60–120 kVp, respectively. At 60 keV, the values were 34.3%, 32.2%, and 31.3% for 80–120 kVp.

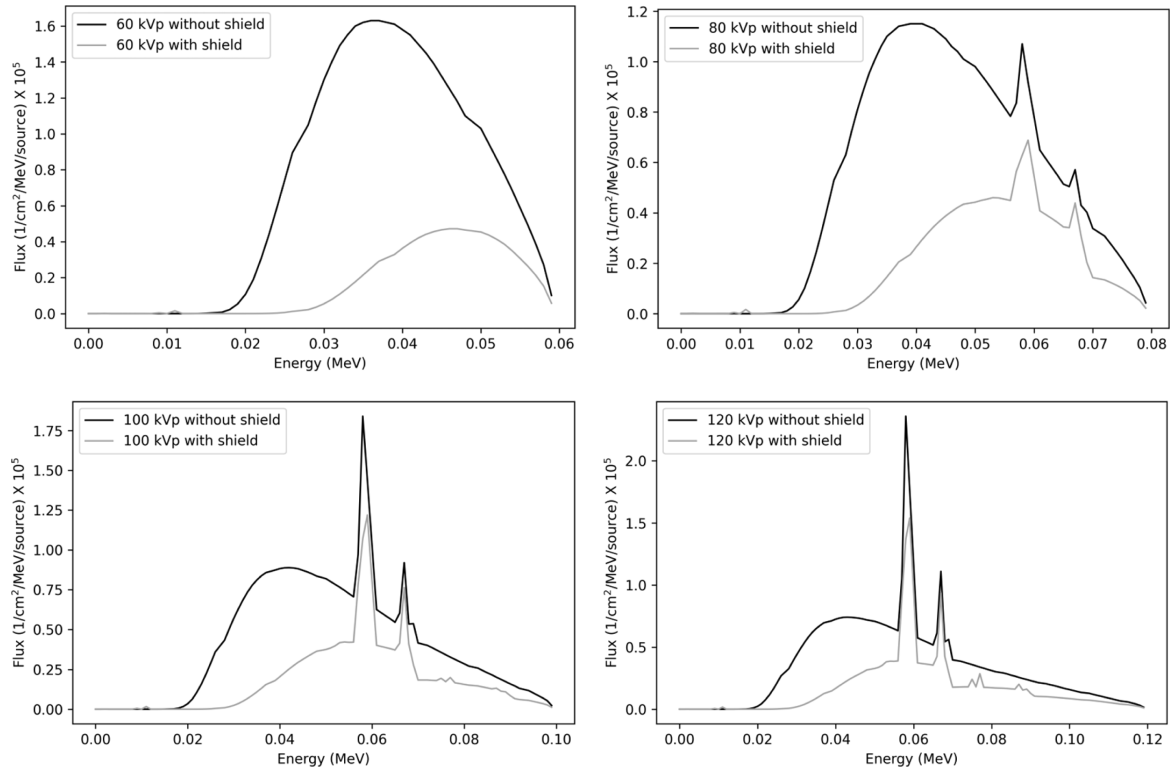

Fig. 6. Energy spectrum variations from PHITS simulations at 60–120 kVp with and without shield.

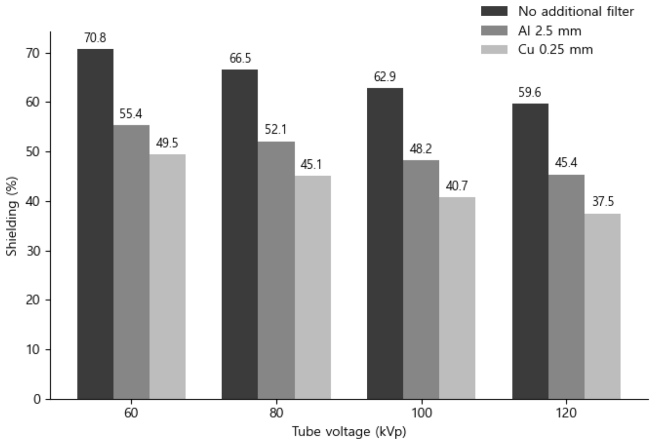

Fig. 7. Shielding efficiency (%) according to tube voltage and additional filtration.

At 70 keV, shielding efficiencies were 53.2%, 49.2%, and 44.6% for 80–120 kVp, and at 80 keV they were 40.9% and 37.9% for 100–120 kVp. At 90 keV, the efficiencies were 51.1% and 49.1% for 100–120 kVp, while at 110 keV, a shielding efficiency of 37.3% was calculated for 120 kVp.

The dose reduction rates at tube voltages of 60, 80, 100, and 120 kVp with 20 mA were measured five times under conditions with and without additional filters, and the average values were plotted as bar graphs, as shown in Fig. 7.

In the absence of additional filters, the shielding efficiencies were 70.8% at 60 kVp, 66.5% at 80 kVp, 62.9% at 100 kVp, and 59.6% at 120 kVp, indicating that the shielding efficiency decreased by approximately 3.7% for every 20 kVp increase in tube voltage. As the tube voltage increased, the shielding efficiency with the 2.5 mm Al filter decreased from 55.4% to 45.4%, showing a reduction of approximately 3.3% for every 20 kVp increase. Similarly, with the 0.25 mm Cu filter, the shielding efficiency decreased from 49.5% to 37.5%, exhibiting a reduction of approximately 4.0% for every 20 kVp increase. The calculated lead equivalence for all conditions was 0.04 mmPb.

Table 1. Scattered radiation shielding efficiency from the phantom according to shielding layers.

Scattered radiation shielding efficiency (%)					
		60 kVp	80 kVp	100 kVp	120 kVp
1 layer	30 cm	57.9	49.7	44.4	40.4
	50 cm	56.1	47.5	40.7	35.6
1.5 layers	30 cm	79.0	72.9	68.5	65.1
	50 cm	80.2	70.4	64.5	60.8

The scattered radiation shielding efficiencies measured at 30 cm and 50 cm from the primary beam for tube voltages of 60, 80, 100, and 120 kVp according to the number of shield layers are shown in Table 1. Under the 1-layer condition, shielding efficiencies at 30 cm ranged from 40% to 58%, depending on tube voltage. At 50 cm, the values were slightly lower, ranging from 36% to 56%. Under the 1.5-layer condition, shielding efficiencies increased to 65–79% at 30 cm and 61–80% at 50 cm.

3.2. Dose reduction assessment

Table 2 summarizes the quantitative evaluation of dose reduction using a chest phantom under fluoroscopy mode with the Automatic Brightness Control (ABC) function activated. The phantom was positioned such that, without the shield, the ABC system produced tube voltages of approximately 80, 90, and 100 kVp for the respective measurement conditions. When the shield was applied, the ABC function resulted in an average increase of about 3 kVp, while the tube current either remained unchanged or showed slight variations, ranging from an increase of 0.6 mA to a decrease of 0.1 mA.

The measured doses without the shield were 7.03, 4.73, and 9.10 μSv, whereas with the shield they decreased to 4.93, 3.27, and 6.75 μSv, respectively. The corresponding relative dose reduction rates were 29.8%, 30.9%, and 26.1%, yielding an average reduction of approximately 29%.

Table 2. ABC-induced tube parameter changes and shielding dose reduction.

Phantom	Shielding	Voltage (kVp)	Current (mA)	Dose (μSv)	Dose difference (%)
Chest	Without shield	82	4.3	7.03 ± 0.35	–
	With shield	86	4.9	4.93 ± 0.57	29.8% reduction
	Without shield	88	4.8	4.73 ± 0.50	–
	With shield	90	4.8	3.27 ± 0.17	30.9% reduction
	Without shield	99	4.4	9.10 ± 0.01	–
	With shield	102	4.3	6.75 ± 0.12	26.1% reduction

Table 3. Quantitative SNR and CNR measurements with and without the composite shield.

Parameter	Without shield	With shield	Difference	Paired t-test (p-value)	Wilcoxon test (p-value)
SNR	35.97 ± 6.88	35.40 ± 5.61	-1.56%	0.68	0.81
CNR	10.52 ± 4.89	11.33 ± 4.51	7.60%	0.52	0.81

3.3. Quantitative Evaluation of Image Quality

The quantitative evaluation results based on SNR and CNR values are presented in Table 3. The SNR decreased slightly from 35.97 without the shield to 35.40 with the shield, whereas the CNR increased from 10.52 to 11.33 under the same conditions. Statistical analysis of the differences in SNR and CNR before and after applying the shield showed no significant differences using either the paired t-test or the Wilcoxon signed-rank test ($p > 0.05$).

4. Discussion

The attenuation characteristics of the composite shield depend on the atomic number and density of its constituent materials, as well as the energy of the incident photons—that is, the mass attenuation coefficient [22].

The composite used in this study, consisting of tungsten, tungsten carbide, bismuth, aluminum, and polyurethane, was designed by combining high-Z metals with a low-density polymer to achieve efficient attenuation of low-energy X-rays, which are relatively unnecessary for diagnostic image acquisition. According to the PHITS-based Monte Carlo simulation results, the dose reduction rate gradually decreased from approximately 77% to 52% as the tube voltage increased from 60 kVp to 120 kVp. This trend can be explained by the decrease in the mass attenuation coefficient with increasing X-ray energy. The mass attenuation coefficient represents the attenuation capability per unit mass and reflects the combined probabilities of interactions such as the photoelectric effect and Compton scattering. In general, as photon energy increases, the contribution of the photoelectric effect diminishes while Compton scattering becomes more dominant, resulting in a reduction in μ/ρ and consequently lower attenuation efficiency [23, 24]. In other words, at high energies, X-ray penetration increases even when the shield thickness remains constant.

The experimentally measured shielding efficiencies were consistent with these theoretical trends. In the absence of additional filtration, the shielding efficiency ranged from 70.8% to 59.6% across 60–120 kVp, while the application of a 2.5 mm Al filter and a 0.25 mm Cu filter resulted in efficiencies of 55.4–45.4% and 49.5–37.5%, respectively. These findings are comparable to dose-reduction results reported in previous studies on barium-based shielding materials [25]. The reduced attenuation efficiency with added filtration can be attributed to the removal of low-energy photons, which increases the average X-ray energy and consequently decreases the shielding effect. In other words, the composite shield exhibits relatively high attenuation in the low- to mid-energy range, but its performance gradually decreases at higher energies, consistent with the general attenuation behavior of diagnostic X-rays.

Although the scattered radiation shielding efficiency showed a slight decrease with increasing tube voltage, consistent attenuation performance was observed across all energy ranges. Even a single layer demonstrated meaningful shielding effects, while the application of 1.5 layers markedly improved overall efficiency, resulting in approximately 60–80% attenuation of scattered radiation. These findings are comparable to, or in some conditions superior to, the approximately 64% attenuation reported by Meisinger *et al.* for staff-protection equipment such as table skirts and ceiling-suspended shields, suggesting that the proposed lead-free composite shield can effectively attenuate primary scattered radiation in regions adjacent to the patient. Therefore, this shield has strong clinical potential as a supplementary radiation protection tool that can contribute to reducing occupational exposure among medical staff [26].

A recent systematic review by Samara *et al.* reported that the effectiveness of patient contact shielding in medical X-ray imaging is limited, noting that shields may have minimal impact on actual dose reduction and may even increase exposure parameters through interactions with Automatic Exposure Control (AEC), potentially leading to image degradation or repeat examinations [27]. In contrast, the phantom experiment in the present study showed that, under C-arm conditions with the Automatic Brightness Control (ABC) function activated, the tube current—which is directly related to patient dose—remained largely unchanged or even decreased slightly. During ABC-regulated fluoroscopy of the chest phantom, tube current either remained constant or decreased, while dose reduction rates of approximately 26–31% were observed. These findings differ from those of Lee *et al.*,

who reported increases in tube voltage and tube current under AEC mode when using barium composite shields and conventional lead shields, resulting in limited dose reductions of only 20–32% [28]. This suggests that the composite shield used in the present study did not trigger compensatory increases in exposure parameters and was able to maintain its shielding performance without adversely affecting automatic brightness regulation.

In the quantitative evaluation of image quality, the SNR decreased by approximately 1.6% and the CNR increased by about 7.7% compared with the unshielded condition; however, neither change was statistically significant. This contrasts with the findings of Jeon *et al.*, who reported a 26.5% reduction in CNR when using a tungsten–bismuth composite shield, indicating that no degradation in image quality occurred in the present study [29]. These results suggest that the proposed composite shield can reduce patient radiation exposure while preserving diagnostic image quality.

These findings indicate that the composite shield effectively combines the attenuation efficiency of high–atomic number materials with the mechanical flexibility of polyurethane, allowing it to maintain structural advantages such as reduced weight, lead-free composition, and minimal artifact generation, while still providing meaningful dose reduction in practical fluoroscopic settings. Therefore, the composite shield has the potential not only to significantly reduce patient radiation exposure without compromising image quality, but also to decrease occupational exposure for personnel participating in interventional or surgical procedures.

Nonetheless, this study was based on experiments using an in-house phantom and therefore has the limitation of not fully representing actual clinical conditions. Various physiological factors—such as patient body habitus, anatomical structure, respiration, and motion—may influence the attenuation characteristics of the shield. Thus, future clinical studies are necessary to validate its performance under real-world clinical scenarios.

5. Conclusion

Although conventional lead-based and lead-free (e.g., bismuth) shields exhibit high dose-attenuation performance, their clinical utility has been limited by several drawbacks, including discomfort during use, image artifacts, reduced contrast, and increased noise. These issues prevent an adequate balance between patient dose reduction and the preservation of image quality, and numerous previous studies and reports have continued to question their practical effectiveness. In contrast, the composite shield developed in this study integrates high-atomic-number materials (tungsten, tungsten carbide, bismuth metal) with low-density polymers (aluminum, polyurethane), enabling excellent attenuation in the low- to mid-energy range while simultaneously minimizing image quality degradation and scatter effects. Accordingly, the proposed shield demonstrates the ability to address the image degradation and patient dose increase observed with traditional lead and bismuth shields, thereby contributing simultaneously to radiation dose reduction and the preservation of image quality. Future research should include clinical investigations to validate attenuation performance under diverse anatomical conditions (e.g., pelvic, abdominal regions) and varying patient body habitus, ensuring its applicability in real-world clinical environments.

Acknowledgments

This research was supported by the National Research Council of Science & Technology (NST) grant by the Korea government (MSIT) (No. CAP22042-300) & Korea Institute of Radiological & Medical Sciences (KIRAMS) grant funded by the Korea government (Ministry of Sciences and ICT) (No. 50572-2024) & the Nuclear Safety Research Program through the Korea Foundation of Nuclear Safety (KoFONS) using the financial resource granted by the Nuclear Safety and Security Commission (NSSC) of the Republic of Korea (RS-2022-KN071220).

Competing interests statement

The authors declare no competing interests.

References

[1] W. Feng, W. Wang, S. Chen, K. Wu, and H. Wang, International Orthopaedics **44**, 919 (2020).
[2] I. Ojodu, A. Ogunsemoyin, S. Hopp, T. Pohlemann, O. Ige, and O. Akinola, European Journal of Orthopaedic Surgery & Traumatology **28**, 1563 (2018).
[3] J.-H. Kim, G.-J. Kim, S.-J. Yoo, and M.-S. Ju, J. Magn. **28**, 438 (2023).
[4] X. Ou, X. Chen, X. Xu, L. Xie, X. Chen, Z. Hong, H. Bai, X. Liu, Q. Chen, L. Li, and H. Yang, Research 9892152 (2021).
[5] M. Berger, Q. Yang, and A. Maier, Medical Imaging Systems: an Introductory Guide **11111**, 119 (2018).
[6] Y.-S. Ji, J.-H. Kim, and M.-S. Han, J. Magn. **28**, 449 (2023).
[7] B. O'Brien and W. Van der Putten, Radiation Protection Dosimetry **129**, 59 (2008).

[8] M. Balonov and P. Shrimpton, Annals of the ICRP **41**, 129 (2012).
[9] D. Ritter, J. Orman, C. Schmidgunst, and R. Graumann, Computerized Medical Imaging and Graphics **31**, 91 (2007).
[10] J. GuÐjónsdóttir, B. Ween, and D. R. Olsen, Radiologic Technology **81**, 309 (2010).
[11] M. B. Cantlon and A. M. Ilyas, Hand **16**, 505 (2021).
[12] S. Y. Lee, E. Min, J. Bae, C. Y. Chung, K. M. Lee, S.-S. Kwon, M. S. Park, and K. Lee, Spine **38**, 2108 (2013).
[13] M. Endo, Y. Haga, M. Sota, A. Tanaka, K. Otomo, Y. Murabayashi, M. Abe, Y. Kaga, Y. Inaba, and M. Suzuki, Journal of Radiation Research **62**, 414 (2021).
[14] M. G. L. Monaco, A. Carta, T. Tamhid, and S. Porru, International Journal of Environmental Research and Public Health **17**, 5877 (2020).
[15] A. Safari, P. Rafie, S. Taeb, M. Najafi, and S. M. J. Mortazavi, Journal of Biomedical Physics and Engineering **14**, 229 (2024).
[16] Y. M. Lestari, C. Anam, H. Sutanto, Z. Arifin, I. Alkian, I. Suyudi, and G. Dougherty, Biomedical Physics & Engineering Express **9**, 025006 (2023).
[17] V. Saba and M. Keshtkar, Physica Medica **65**, 238 (2019).
[18] R. Tappouni and B. Mathers, International Scholarly Research Notices **2013**, 457396 (2013).
[19] S. Jayakumar, T. Saravanan, and J. Philip, Hybrid Advances **4**, 100100 (2023).
[20] S. Kawauchi, K. Chida, Y. Hamada, and W. Tsuruta, Radiological Physics and Technology **15**, 25 (2022).
[21] AAPM, Policy No. PS 3-B, American Association of Physicists in Medicine (2022). Available at: https://www.aapm.org/org/policies/details.asp?id=3590
[22] I. M. Low and N. Z. N. Azman, Polymer composites and nanocomposites for X-rays shielding. Springer, Newyork, (2020) pp. 1-16.
[23] V. Singh, S. Shirmardi, M. Medhat, and N. Badiger, Vacuum **119**, 284 (2015).
[24] I. Akkurt, B. Mavi, A. Akkurt, C. Basyigit, S. Kilincarslan, and H. Yalim, Journal of Quantitative Spectroscopy and Radiative Transfer **94**, 379 (2005).
[25] H. Cha, K. Lee, M. S. Park, K. M. Lee, K. Cho, and K. H. Sung, Journal of Radiation Research **61**, 705 (2020).
[26] Q. C. Meisinger, C. M. Stahl, M. P. Andre, T. B. Kinney, and I. G. Newton, American Journal of Roentgenology **207**, 745 (2016).
[27] E. T. Samara, N. Saltybaeva, M. S. Merce, S. Gianolini, and M. Ith, Physica Medica **94**, 102 (2022).
[28] J.-W. Lee and D. C. Kweon, Radiation Effects and Defects in Solids **176**, 368 (2021).
[29] H. Jeon, W. C. Shin, H. Y. Seol, Y. Ki, K. B. Kim, K. S. Choo, S. D. Lee, and S.-W. Kang, Journal of Musculoskeletal Trauma **36**, 111 (2023).